
# Rapid Route to Efficient, Scalable, and Robust Perovskite Photovoltaics in Air


| | |
|---|---|
| Journal: | *Energy & Environmental Science* |
| Manuscript ID | EE-ART-04-2018-001065.R1 |
| Article Type: | Paper |
| Date Submitted by the Author: | 15-May-2018 |



| | |
|---|---|
| Complete List of Authors: | Hilt, Florian; Stanford University, Materials Science and Engineering<br>Hovish, Michael; Stanford University, Applied Physics<br>Rolston, Nicholas; Stanford University, Applied Physics<br>Brüning, Karsten; Stanford University<br>Tassone, Christopher; Stanford Synchrotron Radiation Lightsource, Materials Science<br>Dauskardt, Reinhold H.; Stanford University, Materials Science and Engineering |

# Rapid Route to Efficient, Scalable, and Robust Perovskite Photovoltaics in Air

**Authors:** Florian Hilt[1], Michael Q. Hovish[1], Nicholas Rolston[2], Karsten Brüning[3], Christopher J. Tassone[3], Reinhold H. Dauskardt[1*]

**Affiliations:**

[1]Department of Materials Science and Engineering, Stanford University, Stanford, CA 94305, USA

[2]Department of Applied Physics, Stanford University, Stanford, CA 94305, USA

[3]Stanford Synchrotron Radiation Lightsource (SSRL), SLAC National Accelerator Laboratory, Menlo Park, CA 94025, USA

*Correspondence to: dauskardt@stanford.edu

**Abstract**:

We demonstrate a scalable atmospheric plasma route to rapidly form efficient and mechanically robust photoactive metal halide perovskite films in open air at linear deposition rates exceeding 4 cm/s. Our plasma process uses clean dry air to produce a combination of reactive energetic species (ions, radicals, metastables, and photons) and convective thermal energy to rapidly convert the perovskite precursor solution after spray-coating. Such high energy species dissociate the precursor and superheat the solvent, quickly and efficiently curing the perovskite film. Synchrotron X-ray radiation enabled *in-situ* wide angle X-ray scattering (WAXS) measurements with high time resolution. The ultrafast crystallization kinetics are governed by rapid nucleation and growth during the plasma exposure, followed by continued grain growth during cooling. We deposit pinhole-free, robust $CH_3NH_3PbI_3$ films with a ten-fold increase in fracture toughness, a key metric for reliability. Planar devices exhibited remarkably consistent performance with 15.7% power conversion efficiency (PCE) without hysteresis and an improved open-circuit voltage ($V_{OC}$). This excellent performance is attributed to lower defect densities, as measured by external quantum efficiency, steady-state and time-resolved photoluminescence. Large-area devices were made with a strip of 10 samples, and a 13.4% average PCE was measured on a total of 2.4 $cm^2$ electrode area.

**Main text**

Organic-inorganic metal halide perovskites have seen a resurgence in interest due to gains in power conversion efficiency (PCE).[1–6] Perovskite solar cells (PSC), however, suffer from several stability challenges including thermomechanical reliability[7] and moisture sensitivity[8–12], which are not competitive with the stability of c-Si modules and their 25 year-service lifetimes. With respect to fabrication, which represents a major advantage for solution processed PSCs, slot die coating[13] and ambient spray coating[14] have emerged as scalable processes, but like spin-coating, these methods require lengthy anneal times. Further works reported the use of a solvent- and vacuum-free process to produce a 12.1% PCE perovskite solar module, however, the approach requires several steps, including a cumbersome peel process which risks mechanical damage to the fragile absorber layer.[15]

In light of these challenges, we have developed an open air Rapid Spray Plasma Processing (RSPP) method for the rapid deposition of both efficient and mechanically robust perovskite layers. $CH_3NH_3PbI_3$ ($MAPbI_3$) films were sprayed and immediately exposed to a plasma at a linear processing rate of > 4 cm/s to form efficient metal halide perovskite in open air, making it extremely amenable to roll-to-roll manufacturing. The combination of reactive species (ions, radicals, metastables, and photons) and convective thermal energy produced by the plasma rapidly transfer energy to the perovskite-precursor solvate. No additional annealing or post-deposition processing is required. Furthermore, RSPP has a high conversion yield (only 1 $\mu L/cm^2$ of solution required) in contrast to spin coating (up to 50 $\mu L/cm^2$ necessary).

Based on an inverted device architecture, we demonstrate a 15.7% PCE with an improved $V_{OC}$ due to reduced defect concentration. A ten-fold increase in perovskite fracture resistance (~ 4.4 J $m^{-2}$) compared to spin-coated films (~ 0.4 J·$m^{-2}$) was shown and attributed to the polycrystalline grain structure of the film. Using synchrotron radiation, we resolved the rapid crystallization process with *in-situ* wide angle X-ray scattering (WAXS). The evolved by-products of the plasma curing were analyzed with gas-phase mass spectrometry (GPMS). The plasma-precursor interaction leads to efficient removal of solvent and acetate, nucleation of small particles, and subsequent growth and coalescence into grains on the millisecond timescale.

## 1. Processing of $MAPbI_3$

The RSPP system, including an atmospheric plasma post-discharge and ultrasonic spray nozzle, is shown in Fig. 1a. After spraying of the perovskite-forming solution, the plasma post-discharge was immediately scanned over the sprayed mixture to form the perovskite at rates of up to 4 cm/s, allowing substrates as large as 930 $cm^2$ to be rapidly deposited with high quality perovskite films (Fig. 1b). Clean, dry air was used as the plasma gas, promoting a cost-effective plasma process. RSPP has been previously used by our group to fabricate submicron barrier films for improved efficiency and stability of perovskite solar cells.[16]

Optimized conditions were found by adjusting the scan rate of the system, the spray solution concentration and liquid flow rate, and the plasma curing dose including plasma power, gas flow rate and plasma nozzle-substrate distance *a*. The volume of precursor solution deposited was a function of the nozzle-substrate distance *b*, the scan speed and the liquid flow rate. These parameters were optimized to deliver the appropriate volume of liquid for a given plasma exposure. If the liquid volume was too high, the plasma cure would not completely convert to perovskite, if the liquid volume was too low, the plasma cure would degrade the perovskite layer. The plasma curing dose includes the plasma power, gas flow rate and plasma nozzle-substrate distance *a*. Increasing the gas flow rate results in a decrease in the density of reactive species and of the available thermal energy. The optimal plasma nozzle-substrate distance leverages the large gradient in energy density in the plasma post-discharge, as the gas cools and the density of reactive species falls off.

The stoichiometry and chemical composition of the finished films were determined by X-ray photoelectron spectroscopy (XPS, Fig. S1 and S2, ESI). Table S1 (see ESI) displays the relative atomic concentration of the different elements related to Fig. S2a (see ESI). All the films produced from the different conditions contained carbon, nitrogen, lead and iodine, in good agreement with the formation of $MAPbI_3$ films. Intense peaks observed in X-ray diffraction (XRD) at 14.10°, 28.44°, 31.83° and 40.53° correspond to (110), (220), (310) and (224) planes of the tetragonal phase of $MAPbI_3$, respectively (Fig. 1c).[17,18] The reactive species from the plasma were not detrimental to the formation of the $MAPbI_3$ layer and, in fact, produced fully cured and pinhole-free films. The presence of lead iodide ($PbI_2$) is apparent in both the RSPP and spin-coated films from the (001) and (003) peaks at $2\theta$ = 12.70° and 38.40°, respectively.[19,20]

Spin-coated film grain diameters ranged from *ca.* 100 nm to 500 nm (Fig. 2a,b), similar to previously reported results using the same perovskite precursors.[21] In some cases, grain diameters up to 1 μm were observed (Fig. 2a, inset). RSPP films exhibited a polycrystalline

grain structure, apparent in top-down (Fig. 2c) and cross-sections (Fig. 2d). Two distinctive grain sizes were observed in the RSPP films: a smaller distribution of grain sizes similar to the spin-coated controls (Fig. 2a,b) with a slightly smaller average grain size (100-300 nm) and a second distribution of micrometer-sized anisotropic platelets (Fig. 2c, inset). These features are unusual compared to a standard spin-coated film, where individual, block-like grains comprise the entire film thickness. The grain boundaries of the RSPP film did not exhibit any voids that would result in carrier recombination or shunt pathways in a device. The high density of grains and bimodal grain size distribution in RSPP likely arises from the unique synergy between the plasma reactive species and the thermal energy convected by the neutral background gas.

To discriminate the role of the plasma reactive species (ions, radicals, metastables, and photons) and thermal energy in the formation of the perovskite, hot air at the same temperature as the plasma was used to cure the perovskite-forming solution. The uniform surface coverage observed in the RSPP film was in stark contrast to the hot air-cured film, which resulted in poor morphology and pinholes of several hundreds of nanometers in diameter (Fig. 2e). Cross-sections (Fig. 2f) revealed large voids present at the interface of the substrate and the $MAPbI_3$ layer that render a PSC completely inoperable. These results strongly suggest that plasma reactive species contributed to the formation of a uniform perovskite film as discussed later.

## 2. Solar Cell Device: Efficiency and Optical Properties

The photoactive quality of RSPP $MAPbI_3$ was assessed in a solar cell device and compared to a spin-coated control. The device was constructed based on an inverted PSC architecture (Fig. 3a).

Spin-coated $MAPbI_3$ films were deposited by using an optimized solution for this process.[21] The RSPP devices exhibited a best PCE of 15.7% (Fig. 3e) as well as remarkably consistent performances, averaging 13.4% for 10 devices made in one batch (Fig. 7), and 12.6% across 25 devices made in several batches with a standard deviation of 1.8% (Table S2, ESI). This reproducibility was comparable to the spin-coated devices (Table S2, ESI). Both devices prepared from RSPP or spin-coated perovskite presented a hysteresis-free behavior (Fig. S3, ESI).

The best-performing RSPP device exhibited a fill factor (FF) of 0.69, a short-circuit photocurrent density ($J_{SC}$) and open-circuit voltage ($V_{OC}$) of 21.8 mA/cm$^2$ and 1.05 V, respectively. Photocurrent density and voltage were stable at maximum power point, and maximum power point tracking showed a good stability over time (Fig. S4, ESI). It is known that the p-i-n inverted structure based on PEDOT:PSS as HTL entails a significant $V_{OC}$ drop of several hundreds of millivolts compared to other materials such as PTAA and NiO.[22–25] However, RSPP achieved an outstanding gain in $V_{OC}$ of 70 mV compared to the spin-coated control, attaining 1.05 V, among the highest $V_{OC}$ ever measured with PEDOT:PSS as a hole-transporting layer. This increase in $V_{OC}$ was consistent across all RSPP devices (Table S2, ESI) and was associated with differences in the perovskite quality.

Figure 3g shows the absorption spectra of $MAPbI_3$ synthesized from spin-coated and RSPP, both of which exhibited the same absorption features. Steady-state photoluminescence (PL, Fig. 3h) measured a slightly lower band gap for RSPP $MAPbI_3$ (1.61 eV) than for its spin-coated counterpart (1.62 eV). The corresponding external quantum efficiency (EQE, Fig. 3f) were also very similar between both films. EQE had a broad plateau with a maximum value of 85% for spin coating and 87% for RSPP over essentially the entire visible range. The integrated $J_{SC}$ values calculated from EQE (18.78 mA/cm$^2$ for spin coating and 18.73 mA/cm$^2$ for RSPP) matched well with the measured values from the *J-V* curve. A pronounced shoulder around 700 nm can be observed due to reflection phenomena occurring from the PEDOT:PSS layer.

Figure 3i shows the time-resolved PL spectra of the spin-coated and RSPP $MAPbI_3$ films. The PL decay of the films indicated a higher carrier lifetime for the RSPP $MAPbI_3$ than for the spin-coated perovskite. $V_{OC}$ is dependent on both $J_{SC}$ and diffusion length ($L_{diff}$) (Eq. (S1) and (S2), ESI). The current density $J_{SC}$ was relatively close between the two films, therefore, the diffusion length may explain the higher $V_{OC}$ obtained with RSPP. Trap states introduced by defects can cause carrier recombination, creating efficient recombination pathways, negatively impacting the diffusion length. One explanation is the interaction with plasma reactive species resulted in the quenching of trap states during film deposition, leading to longer carrier lifetime and larger diffusion lengths. For example, photo-absorption or surface charging may play a role, although further experimentation will be required to identify any specific mechanism. The results suggest that RSPP perovskite had a lower defect density compared to spin-coated devices.

## 3. Nucleation and Growth Mechanisms

### 3.1 *In-situ* Wide Angle X-ray Scattering

Wide angle x-ray scattering (WAXS) is useful for probing the crystallinity of thin film materials and has been particularly useful in understanding nucleation and growth in metal halide perovskites.[26–29] Given the requirements for resolving the RSPP on a meaningful timescale (*ca.* 10 ms), a synchrotron X-ray source is required. Synchrotron rings can provide fluxes in excess of $10^{12}$ photons/s, at high energies, making them ideal sources for time resolved characterization of formation processes at the fidelity needed to follow nucleation and growth. We integrated the RSPP configuration into endstation 10-2 at the Stanford Synchrotron Radiation Lightsource (SSRL) and performed *in-situ* WAXS to characterize the rapid nucleation and growth of perovskite with a time resolution of 15 ms (Fig. 1d and Fig. S5, ESI).

The evolution of the integrated intensity of the diffraction peak at q = 1.0 1/Å over time is displayed in Fig. 1d. This peak is indexed as (110) in the tetragonal phase and serves as a good proxy for the amount of perovskite present in the film. Over the course of the plasma exposure, there was a rapid increase in the peak area. The crystallization half time is less than 100 ms. Following the exposure, the peak area continued to grow, although at a significantly reduced rate. This continued growth lasts for several seconds. The interplay between these two distinct growth regimes ultimately leads to excellent mechanical and optoelectronic performance, as described below.

Note that the intense x-rays themselves had no effect on perovskite crystallization as no signal was recorded during the x-ray exposure before the plasma cure. This indicated that the sprayed solution was not converted into perovskite without plasma curing even when the sample was exposed to the intense x-rays (Fig. 1d and Fig. S5b, ESI).

### 3.2. Plasma reactive species and convective energy

Plasma energy involves synergistic contributions from reactive species (ions, radicals, metastables, and photons) and convective thermal energy. *In-situ* spectroscopy and thermal measurements were used to determine the extent to which these contribute to perovskite formation.

Free radical and excited metastable species, such as nitric oxide (NO), atomic nitrogen (N), and atomic oxygen (O) (Fig. 4b,c and Fig. S4, see ESI, as determined from optical emission and mass spectrometry), each carry a significant amount of internal energy (> 1 eV), which can dissociate and volatilize solvent molecules. Photons provide another source of energy (Fig. 4b), generated by radiative de-excitation from the atomic and molecular radicals, and metastable species. The thermal energy is defined by the background gas temperature, *i.e.* the temperature of the electrically neutral species within the plasma. This energy is transferred to the precursor-solvate through convection as shown by the large Rayleigh number (~ $10^6$, Eq. (S3), ESI).

The plasma passed over the sample for a total exposure of 250 ms, during which time, the temperature rose rapidly to 152°C (Fig. 1d). The flux of these reactive species rapidly increased during the plasma exposure. As the plasma post-discharge moved away from the sample, the density of reactive species dropped abruptly, and the film was cooled to room temperature (Fig. 1d).

We next elucidate how the combination of reactive species (ions, radicals, metastables, and photons) and thermal energy affect the steps that govern the nucleation and growth of the perovskite during RSPP.

### 3.3. Solvent evaporation and supersaturation

The plasma anneal lead to superheating and rapid removal of the solvent. When sampling the volatilized compounds during RSPP, *in-situ* gas phase mass spectrometry (GPMS) detected the rapid evolution of DMF, acetate, and methyl amine (Fig. 4a). From the evolved gas analysis, it was apparent that the acetate dissociated from the salt and was volatilized during the cure. The evolution of methylamine from the solution was expected, as there was a molar excess of methylammonium iodide (MAI) in solution based on previously optimized methods.[21]

Radicals that involve reactive oxygen and nitrogen species (RONS) are known to play a key role during plasma-liquid interactions. *In-situ* gas-phase mass spectrometry (GPMS) revealed the presence of $N^{\bullet}$, $O^{\bullet}$, $NO^{\bullet}$ and $^{\bullet}OH$ radicals at the substrate in the case of RSPP (Fig 4c). Free radicals produced by the plasma were convectively transported to the sprayed liquid by the gas flow and forced convection enhanced the mass transfer of the radicals through the perovskite precursor-solvate. Models showed that RONS may penetrate a liquid and react to a

depth from 10 to 100 μm.[30] Given the thin nature of these wet precursor films (~ 1 μm), the radical species would have access to the entire depth of the film, diffusing through the plasma-liquid interface.

The system can gain additional thermal energy if the optical emission of the plasma aligns well with the absorption spectrum of the solvent. The NOγ system emitted by the air plasma produces deep UV photons ($200 < \lambda < 300$ nm), which coincide with the absorption peak of DMF (Fig. 4d). When UV light is absorbed by DMF, excited electrons are quickly quenched, and the optoelectronic energy is transferred to thermal energy.

The synergistic effect of these mechanisms resulted in rapid and efficient removal of solvent and acetate molecules. As the system undergoes supersaturation, the precursor-solvate contracts and concentrates, in an analogous manner to spin-coating. During and following supersaturation, perovskite crystallites begin to nucleate and grow.

### 3.4. Charge enhanced nucleation and growth

Here, we consider how the combination of reactive species (ions, radicals, metastables, and photons) and thermal energy can promote the nucleation and growth of the perovskite film during RSPP.

It has recently been reported that illumination can enhance the rate of perovskite formation[31] by lowering the surface energy between the growing crystallite and the precursor-solvate. This phenomenon is a derivative of electrowetting—aptly named photo-electrowetting (PEW)—observed at an electrolyte/semiconductor interface and is reported for other photovoltaic materials like silicon.[32] Incident light above the semiconductor's bandgap generates free carriers, which modifies the system's electric potential.[31] The addition of electrical energy modifies the surface energy according to the Lippmann equation (Eq. (1)):

$$\gamma - \gamma_0 = -\frac{1}{2} \cdot \frac{1}{A} \cdot \frac{Q^2}{C_0} \qquad (1)$$

where $\gamma$ is the surface energy in the presence of charge, $\gamma_0$ is the uncharged surface energy, Q is the excess charge at the surface of the semiconductor, A is the surface area, and $C_0$ is the capacitance of the structure. The change in surface energy depends on the square of the excess surface charge. An interesting consequence of this quadratic dependence is the contribution of both positive and negative excess surface charge, meaning that any charged species can contribute to the change in surface energy. In the case of RSPP, not only photo-generated

carriers can contribute as recently reported,[31] but reactive species (ions, radicals, metastables and photons) can participate through diffusion but also reactions with the liquid, generating additional charged species.[30] The spectral irradiance under an AM1.5G solar spectrum for photon energy ≥1.5 eV can be estimated to be ~ 500 $W \cdot m^{-2}$ at most, without considering any potential loss of photon density from reflection, scattering, and absorption. In the case of RSPP, and in addition to spectral irradiance from the plasma (estimated to be ~ 1.5 $W \cdot m^{-2}$, Fig. 4b,S6), reactive species from the plasma with high electron and ion density[30] (*i.e.* $10^{18}$-$10^{19}$ $m^{-3}$ each), radical density[30] (*i.e.* $10^{21}$-$10^{23}$ $m^{-3} \cdot s$), and metastables density (≥$10^{10}$ $m^{-3}$), effectively introduce charged species, further lowering the activation energy of grain nucleation and enhancing the rate of perovskite nucleation and growth (Fig. 5). The change in surface energy is dependent on the number of excess charge and is all the more pronounced as the particle radius is small (Fig. 5b).

According to classical homogenous nucleation theory, the free energy of a growing particle is given by Eq. (S6) (ESI) and a particle is considered stable when R > R*, where R* is the critical radius associated with ΔG*, the energy barrier to nucleation (Eq. (S7), ESI). Combining Eq. (1) and Eq. (S7) (ESI), we arrive at Eq. (2) for the nucleation barrier associated with plasma annealing:

$$\Delta G^*_{RSPP} = \frac{16\pi}{3g_v^2}\left(\gamma_0 - \frac{1}{2}\cdot\frac{1}{A}\cdot\frac{Q^2}{C_0}\right)^3 \qquad (2)$$

where $g_v$ is the free energy associated with the bulk volume.

Figure 5c represents the ratio of the activation barrier of the charged surface ($\Delta G^*_{RSPP}$) to the uncharged surface ($\Delta G^*_{Thermal}$) as a function of the number of excess surface charges. For small nuclei (r < 1 nm), even a few excess surface charges can significantly lower the activation barrier. The effect is less pronounced for larger particles (r ≥ 5 nm), as the bulk Gibbs free energy begins to dominate over any change in surface energy arising from charging. These numbers suggest that very small quantities of excess surface charge can significantly decrease the nucleation barrier, reduce the critical radius, and increase the number of stable nuclei.

Mass spectrometry and optical emission spectroscopy indicated a significant amount of radicals, metastables, and photons emitted by the plasma. The plasma generated reactive species created excess charge at the surface of the semiconductor particle, lowering the surface energy and stabilizing small nuclei against dissolution. This is evinced by the high density of grains observed both in the plane of the film (Fig 2c).

The large, irregular grains observed in SEM (Fig. 2c, inset) likely arose from grain growth, during the reduced growth rate regime observed in the *in-situ* WAXS. For example, small quantities of precursor solvate may remain in the grain boundaries of the perovskite following the plasma exposure. As the sample cools, it becomes less favorable for new particles to nucleate. Instead, the precursor-solvate is consumed by larger grains, which have more favorable kinetics. This can result in grain growth, and the stitching together of many small grains into one, larger grain. These large grains are scattered throughout the film, apparent in top-down SEM (Fig. 2c, inset). The RSPP couples charge enhanced nucleation and growth with grain growth, to create a bimodal grain distribution which is robust against mechanical degradation.

In order to determine the grain growth mode discussed above during the transformation phase (Fig. 1d), the Avrami approach was applied (see ESI, Equation S9). Usually, transformation kinetics from amorphous to crystalline phase can be described at constant temperature by plotting a derivation of the Avrami equation (see ESI, Equation S9) and extracting the Avrami exponent *n*. Here, the Avrami analysis was integrated over the temperature of the plasma during the curing (Fig. 1d) by inserting an Arrhenius-like temperature dependence for the crystallite growth rate into the derivation of the Avrami equation (see ESI, Equation S9). Accounting for the changing temperature (Fig. 1d), an Avrami coefficient of $n = 0.5$ was found—which clearly indicates a crystallization assisted by unidirectional (1D) diffusion processes that can result to an increase of the crystal domain size in the film—consistent with what we observed previously (Fig. 2c inset,d). This differs from classic thermal annealing process and is similar to previously reported results under different UV-induced crystallization conditions[33], which corroborates the role of reactive species in the fast crystallization of a polycrystalline grain structure.

All the evidences discussed above indicate that during RSPP, photo-generated (1.5 $W \cdot m^{-2}$ for RSPP as compared to 500 $W \cdot m^{-2}$ under a 1 sun AM1.5G[31]) and convective thermal energy (Fig. 2e,f) are not sufficient on their own to promote the fast crystallization of perovskite, and that charged species introduced by the plasma are critical to achieve such crystallization rate of high quality perovskite.

## 4. Mechanical Properties

The fracture energies ($G_c$) of the $MAPbI_3$ perovskite thin films are known to be extremely low ($G_c$ values typically <1.5 $J \cdot m^{-2}$).[7] From decades of research in microelectronic devices, most standard processes in the semiconductor industry require $G_c$ in excess of 5 $J \cdot m^{-2}$ in order to withstand device manufacturing and maintain product longevity, which highlights a real concern over the mechanical reliability of these perovskite systems. Given the quick ascent to efficiencies comparable to c-Si cells, it stands that the most important challenge for the scaling of PSC will be in their thermomechanical reliability and degradation.

The $G_c$ of the RSPP perovskite was compared to a spin-coated film and to a hot-cast film[34] (Fig. 6a), the latter being the most robust planar perovskite reported to date.[7] The fracture energies of the prepared cells were determined using the double-cantilever beam (DCB) test. XPS analysis of the fracture surfaces revealed that the failure occurred cohesively within the perovskite layer (Fig. 6b,c). The $G_c$ values ranged from 0.43 $J \cdot m^{-2}$ for the spin-coated perovskite to 4.4 $J \cdot m^{-2}$ for the RSPP film (Fig. 6a), which is a 10-fold increase and the highest fracture toughness ever reported for an organic-inorganic perovskite film[7] without a mechanically reinforcing scaffold.[35]

The remarkable fracture resistance of RSPP perovskite can be explained by its unique morphology (Fig. 2d). The rapid curing induced a polycrystalline structure in the perovskite film, where crystallites may interlock more effectively. The random orientation and range of grain sizes resulted in a tortuous fracture path, driving up the energy needed to propagate the crack. Crack meandering around large grain features in the RSPP perovskite improved the toughness compared to the more homogeneous crack path that occurred in the uniform, small-grain control films (Fig. S7, ESI). These results suggest that intrinsic toughening mechanisms used in other crystalline materials (dislocation management, twinning, grain size distributions, etc.) may provide a means for making more robust perovskites, opening avenues for reliable and durable flexible architectures.

## 5. Large-scale devices

The scalability of RSPP was assessed by fabricating larger area devices. Considering the substrate area limitation we faced due to the deposition of PEDOT:PSS by spin coating, we lined up 10 regular-size substrates (2×2 $cm^2$) to simulate a large area device with a total electrode area of 2.4 $cm^2$. Figure 7a shows the photograph representing 10 devices lined up and coated with perovskite by RSPP. The total deposition process occurred in air in 7 seconds

(Supplementary Video). The best device showed a 15.7% PCE as discussed previously. By averaging the electrodes area and the PCE for each of them, we obtained a PCE average of 13.4% (± 1.7%) for a 2.4 $cm^2$ electrode area. We attribute the variation not to non-uniformity in the RSPP of the perovskite layer (Fig. S8, ESI), but to subsequent layers non-uniformity and/or possible damages that could have affected the samples during handling. Note that the variation in the performance parameters of RSPP is similar to the spin-coating ones (Table S2).

## Conclusion

A pathway towards fast, scalable fabrication of efficient and mechanically robust perovskite films is demonstrated. *In-situ* wide angle X-ray scattering revealed crystallization on the order of 100 ms. RSPP of perovskite is governed by superheating the perovskite precursor-solvate, charge enhanced nucleation and growth of crystallites, and grain coalescence. The plasma process resulted in one of the toughest films ever measured to date, with a significant increase in fracture resistance, a key metric for reliability. The enhanced mechanical performance is accredited to the bimodal grain distribution. The large, irregular grains grown during coalescence deflect an approaching crack, increasing the film's resistance to mechanical failure.

Devices fabricated with RSPP obtained 15.7% PCE and a $V_{OC}$ of 1.05 V in an inverted PSC. RSPP $MAPbI_3$ showed higher carrier lifetime than spin-coated perovskite. The favorable optoelectronic properties are attributed to a lower concentration of defects in the RSPP perovskite. RSPP enabled rapid deposition of high-quality perovskite films on large-scale substrates with high efficiencies and low deviations. Further increases in PCE are anticipated by incorporating multiple cation species into the perovskite structure. Cesium and formamidinium, for instance, may contribute to greater thermal and moisture resistance, in addition to higher efficiencies, despite fabrication in ambient.[36,37]

## Acknowledgements

This material is based upon work supported by the Department of Energy through the Bay Area Photovoltaics Consortium under Award Number DE-EE0004946. Part of this work was performed at the Stanford Nano Shared Facilities (SNSF), supported by the National Science Foundation under award ECCS-1542152. Additional support was provided by the National

Science Foundation Graduate Research Fellowship, awarded to N. Rolston under award DGE-1656518. Use of the Stanford Synchrotron Radiation Lightsource SLAC National Accelerator Laboratory, is supported by the U.S. Department of Energy, Office of Science, Office of Basic Energy Sciences under Contract No. DE-AC02-76SF00515. We also thank the McGehee group for the use of their facilities and B. A. Reeves for his help and proficiency with TR-PL.

## Author Contributions

F.H., M.Q.H. and N.R. conceived the experiments, data analysis and interpretation. F.H. and M.Q.H. carried out the RSPP. N.R. performed the devices fabrication, device performance measurements and characterizations. F.H. performed the SEM measurements. M.Q.H. performed the XRD analyses. F.H. and M.Q.H. performed the gas phase mass spectrometry and OES study. F.H. performed the XPS analyses. F.H., M.Q.H. and N.R. performed the fracture measurements. M.Q.H. performed the UV-visible measurement. F.H., M.Q.H., N.R. and K.B. performed the WAXS experiments. C.J.T. helped to plan and supervise the *in-situ* WAXS experiments. The project was supervised by R.H.D. All authors contributed to the writing of the paper.

## Competing Financial Interests statement

The authors declare no competing financial interest.

## References

1. A. Kojima, K. Teshima, Y. Shirai, T. Miyasaka, *J. Am. Chem. Soc.*, 2009, **131,** 6050–6051.
2. H. J. Snaith, *J. Phys. Chem. Lett.*, 2013, **4,** 3623−3630.
3. M. A. Green, A. Ho-Baillie, H. J. Snaith, *Nat. Photonics*, 2014, **8,** 506–514.
4. M. Grätzel, *Nat. Mater.*, 2014, **13,** 838–842.
5. J. Berry, T. Buonassisi, D. A. Egger, G. Hodes, L. Kronik, Y.-L. Loo, I. Lubomirsky, S. R. Marder, Y. Mastai, J. S. Miller, D. B. Mitzi, Y. Paz, A. M. Rappe, I. Riess, B. Rybtchinski, O. Stafsudd, V. Stevanovic, M. F. Toney, D. Zitoun, A. Kahn, D. Ginley,

D. Cahen, *Adv. Mater.*, 2015, **27,** 5102–5112.

6. W. S. Yang, B.-W. Park, E. H. Jung, N. J. Jeon, Y. C. Kim, D. U. Lee, S. S. Shin, J. Seo, E. K. Kim, J. H. Noh, S. II Seok, *Science*, 2017, **356,** 1376–1379.

7. N. Rolston, B. L. Watson, C. D. Bailie, M. D. McGehee, J. P. Bastos, R. Gehlhaar, J.-E. Kim, D. Vak, A. T. Mallajosyula, G. Gupta, A. D. Mohite, R. H. Dauskardt, *Extreme Mechanics Letters*, 2016, **9**, 353-358.

8. J. A. Christians, P. A. M. Herrera, P. V. Kamat, *J. Am. Chem. Soc.*, 2015, **137,** 1530–1538.

9. J. Yang, B. D. Siempelkamp, D. Liu, T. L. Kelly, *ACS Nano*, 2015, **9,** 1955–1963.

10. Y. Han, S. Meyer, Y. Dkhissi, K. Weber, J. M. Pringle, U. Bach, L. Spiccia, Y.-B. Cheng, *J. Mater. Chem. A*, 2015, **3,** 8139–8147.

11. H. Gao, C. Bao, F. Li, T. Yu, J. Yang, W. Zhu, X. Zhou, G. Fu, Z. Zou, *ACS Appl. Mater. Interfaces*, 2015, **7,** 9110–9117.

12. S. R. Raga, M.-C. Jung, M. V. Lee, M. R. Leyden, Y. Kato, Y. Qi, *Chem. Mater.*, 2015, **27**, 1597–1603.

13. K. Hwang, Y.-S. Jung, Y.-J. Heo, F. H. Scholes, S. E. Watkins, J. Subbiah, D. J. Jones, D.-Y. Kim, D. Vak, *Adv. Mater.*, 2015, **27,** 1241–1247.

14. S. Das, B. Yang, G. Gu, P. C. Joshi, I. N. Ivanov, C. M. Rouleau, T. Aytug, D. G. Geohegan, K. Xiao, *ACS Photonics*, 2015, **2,** 680–686.

15. H. Chen, F. Ye, W. Tang, J. He, M. Yin, Y. Wang, F. Xie, E. Bi, X. Yang, M. Grätzel, L. Han, *Nature*, 2017, **550,** 92–95.

16. N. Rolston, A. D. Printz, F. Hilt, M. Q. Hovish, K. Brüning, C. J. Tassone, R. H. Dauskardt, *J. Mater. Chem. A*, 2017, **5**, 22975-22983.

17. T. Oku, in *Solar Cells - New Approaches and Reviews*, ed. Kosyachenko, Los Angeles, 2015.

18. X. Guo, C. McCleese, C. Kolodziej, A. C. S. Samia, Y. Zhao, C. Burda, *Dalton Trans.*, 2016, **45,** 3806–3813.

19. Z. Zheng, A. Liu, S. Wang, Y. Wang, Z. Li, W. M. Lau, L. Zhang, *J. Mater. Chem.*, 2005, **15,** 4555–4559.

20. J. F. Condeles, R. A. Ando, M. Mulato, *J. Mater. Sci.*, 2008, **43,** 525–529.

21. W. Zhang, M. Saliba, D. T. Moore, S. K. Pathak, M. T. Hörantner, T. Stergiopoulos, S. D. Stranks, G. E. Eperon, J. A. Alexander-Webber, A. Abate, A. Sadhanala, S. Yao, Y. Chen, R. H. Friend, L. A. Estroff, U. Wiesner, H. J. Snaith, *Nat. Commun.*, 2015, **6,** 1–10.

22. Q. Chen, N. De Marco, Y. Yang, T.-B. Song, C.-C. Chen, H. Zhao, Z. Hong, H. Zhou, Y. Yang, *Nano Today*, 2015, **10,** 355–396.

23. L. Meng, J. You, T.-F. Guo, Y. Yang, *Acc. Chem. Res.*, 2016, **49,** 155–165.

24. C. Bi, Q. Wang, Y. Shao, Y. Yuan, Z. Xiao, J. Huang, *Nature Commun.*, 2015, **6,** 7747.

25. J. You, L. Meng, T.-B. Song, T.-F. Guo, Y. Yang, W.-H. Chang, Z. Hong, H. Chen, H. Zhou, Q. Chen, Y. Liu, N. De Marco, Y. Yang, *Nature Nanotechnol.*, 2015, **11,** 75–82.

26. L. Dou, A. B. Wong, Y. Yu, M. Lai, N. Kornienko, S. W. Eaton, A. Fu, C. G. Bischak, J. Ma, T. Ding, N. S. Ginsberg, L.-W. Wang, A. P. Alivisatos, P. Yang, *Science*, 2015, **349,** 1518–1521.

27. J. Schlipf, P. Docampo, C. J. Schaffer, V. Körstgens, L. Biessmann, F. Hanusch, N. Giesbrecht, S. Bernstorff, T. Bein, P. Müller-Buschbaum, *J. Phys. Chem. Lett.*, 2015, **6,** 1265–1269.

28. T. Miyadera, Y. Shibata, T. Koganezawa, T. N. Murakami, T. Sugita, N. Tanigaki, M. Chikamatsu, *Nano Lett.*, 2015, **15,** 5630–5634.

29. J. Schlipf, P. Müller-Buschbaum, *Adv. Energy Mater.*, 2017, **7,** 1–10.

30. P. J. Bruggeman, M. J. Kuschner, B. R. Locke, J. G. E. Gardeniers, W. G. Graham, D. B. Graves, R. C. H. M. Hofman-Caris, D. Maric, J. P. Reid, E. Ceriani, D. Fernandez Rivas, J. E. Foster, S. C. Garrick, Y. Gorbanev, S. Hamaguchi, F. Iza, H. Jablonowski, E. Klimova, J. Kolb, F. Krcma, P. Lukes, Z. Machala, I. Marinov, D. Mariotti, S. Mededovic Thagard, D. Minakata, E. C. Neyts, J. Pawlat, Z. Lj. Petrovic, R. Pflieger, S. Reuter, D. C. Schram, S. Schröter, M. Shiraiwa, B. Tarabová, P. A. Tsai, J. R. R. Verlet, T. von Woedtke, K. R. Wilson, K. Yasui, G. Zvereva, *Plasma Sources Sci. Technol.*, 2016, **25,** 1–59.

31. A. Ummadisingu, L. Steier, J.-Y. Seo, T. Matsui, A. Abate, W. Tress, M. Grätzel, *Nature*, 2017, **545**, 208–212.

32. S. Arscott, *Sci. Rep.*, 2011, **1,** 1–7.

33. S. J. Park, A. R. Kim, J. T. Hong, J. Y. Park, S. Lee, Y. H. Ahn, *J. Phys. Chem. Lett.*, 2017, **8**, 401-406.

34. W. Nie, H. Tsai, R. Asadpour, J.-C. Blancon, A. J. Neukirch, G. Gupta, J. J. Crochet, M. Chhowalla, S. Tretiak, M. A. Alam, H.-L. Wang, A. D. Mohite, *Science*, 2015, **347,** 522–525.

35. B. L. Watson, N. Rolston, A. D. Printz, R. H. Dauskardt, *Energy Environ. Sci.*, 2017, **10**, 2500-2508.

36. J.-W. Lee, D.-H. Kim, H.-S. Kim, S.-W. Seo, S. M. Cho, N.-G. Park, *Adv. Energy Mater.*, 2015, **5,** 1501310.

37. M. Saliba, T. Matsui, J.-Y. Seo, K. Domanski, J.-P. Correa-Baena, M. K. Nazeeruddin, S. M. Zakeeruddin, W. Tress, A. Abate, A. Hadfeld, M. Grätzel, *Energy Environ. Sci.*, 2016, **9,** 1989–1997.

## Methods

### Materials and solution preparation.

Methylammonium iodide (MAI) was purchased from Dyesol and used as received. Lead acetate trihydrate ($PbAc_2 \cdot 3H_2O$, 99.999%, CAS: 6080-56-4) and hypophosphorous acid (HPA) solution (50 wt.% in water) were purchased from Sigma-Aldrich. The preparation of the perovskite solution consists in dissolving MAI and $PbAc_2 \cdot 3H_2O$ (molar ratio of 3:1) in anhydrous *N,N*-Dimethylformamide (DMF, anhydrous, 99.8%) at a total concentration of 35.7 wt.%. Subsequently, an HPA:DMF (1:100 volumetric ratio) solution was added in the resulted perovskite solution at a concentration of 3.7 wt.%. The solution was stirred and filtered before use.

### Perovskite layer deposition.

Rapid Spray Plasma Process (RSPP).

RSPP perovskite films were synthesized using an atmospheric plasma deposition system provided by Plasmatreat GmbH (Hayward, CA, USA). The atmospheric pressure plasma jet

system used in this study is based on the blown-arc discharge configuration. The arc discharge is produced between two coaxial electrodes and blows out of a nozzle by the main process gas flow (air) at a flow rate of 30 standard liters per minute (slm). The high-voltage electrode was driven by a DC power supply at an excitation frequency of 21 kHz. The resulting arc current was measured to be 18.0 A. The perovskite solution was sprayed onto the substrates in ambient air using a 120 kHz ultrasonic atomizing nozzle (AccuMist, Sono-Tek Corporation) operating at 1.0 W, an atomizing gas pressure of 1 psi and fed by a syringe pump delivering 200 $\mu L \cdot min^{-1}$. The mean diameter of the produced droplets was 25 μm. The deposited liquid layers were quickly (0.25 seconds) exposed to the atmospheric plasma jet system to promote the curing of the sprayed solution. The substrates were placed at a distance $a$ = 4.0 cm from the plasma nozzle. The spray nozzle-to-substrate distance ($b$, Fig. 1a) and the plasma nozzle-to-spray nozzle distance ($c$, Fig. 1a) were kept at a distance of 5 cm and 8 cm, respectively. The moving speed of the nozzles were kept constant at 40 mm/s and 1 pass was performed. The overall procedure was carried out in an open-air enclosure at *ca.* 25°C and 40% R.H. A type K thermocouple was placed in direct contact with the top of the substrate to obtain the most accurate measure of the deposited film temperature.

Hot air.

Hot air-cured perovskite films were synthesized using a stainless-steel tube with an internal diameter (I.D.) identical to the one of the plasma nozzle. Air was heated to 155°C (± 5°C) and passed through the tube at a flow rate of 30 slm to match the same temperature and flow rate that are used for the plasma. All the other parameters are the same that are used with the plasma post-discharge.

Spin-coated deposition.

Spin-coated perovskite films were synthesized from the same precursor materials and concentrations. The solution was filtered and spun at 2000 rpm for 60 s with a 2000 rpm/s ramp rate with a constant stream of dry air directed at the sample to aid solvent evaporation. The films were dried at room temperature then annealed at 100 °C for 5 min in dry air to complete the formation of the perovskite layer.

*In*-situ wide angle X-ray scattering:

The measurements were made at the Stanford Synchrotron Radiation Lightsource (SSRL), beam-line 10-2. The RSPP was integrated into the beam-line, such that the X-rays scattered orthogonal to the cure direction (Fig. S3a, ESI). An X-ray energy of 12.7 keV, an exposure time of 10 ms per frame and an exposure period of 15 ms were used. The incident angle was 3°, with a Pilatus 100K detector placed 23 cm from the sample. Q-space between 0.3 $A^{-1}$ and 42.5 $A^{-1}$ was probed. $LaB_6$ was used to calibrate peak positions.

**Device fabrication.**

Devices were fabricated on ITO-coated glass (Xin Yan Technology, sheet resistance 10 Ω/□). Substrates were then cleaned sequentially in 1:10 Extran:DI water solution followed by sequential sonication and rinsing with DI water, acetone, and IPA. Samples were exposed to UV−Ozone for 15 min to remove any organic residue. A hole transporter layer of PEDOT:PSS (Clevios Al 4083) was then immediately spin-coated at 4000 rpm for 30 s and dried at 135°C for 15 min. The perovskite layer was formed and then the samples were transferred to an $N_2$ glovebox for evaporation (Angstrom Åmod) of the subsequent layers. Buckminsterfullerene ($C_{60,}$ MER Corporation) was deposited at a rate of 0.3 $Å \cdot s^{-1}$. Bathocuproine (BCP, TCI) was deposited at a rate of 0.2 $Å \cdot s^{-1}$. Ag deposition (150 nm) was performed through a shadow mask to define the top electrode.

**Film and device characterization.**

XRD patterns were measured on an X'PERT PRO diffraction system (PANanalytic) equipped with Cu-Kα radiation (λ = 1.5406 Å). 2θ-ω scans were recorded in a Bragg-Brentano geometry, with a step size of 0.01° and dwell time of 500 ms for $10º < 2\theta < 50º$. A baseline correction was applied to all spectrums to remove the broad feature associated with the glass substrate.

X-ray photoelectron spectroscopy (XPS) measurements were carried out on a PHI 5000 Versaprobe instrument (Physical Electronics Inc., US) equipped with a hemispherical energy analyzer and a monochromatic Al($K_\alpha$) X-ray source (hv = 1486.6 eV) operated at 50 W. The pass energy was fixed at 117.4 eV for survey scans and 23.5 eV for core level spectra, with an analysis area of Ø = 200 $\mu m^2$. The XPS spectra were processed with CasaXPS software and a

Shirley-type background was subtracted from the spectra. Peaks were fitted with a Gaussian/Lorentzian (70-30%) line shape.

Scanning electron microscopy (SEM) was performed on a FEI Magellan 400 XHR FE-SEM. Prior to SEM observations, the device samples were coated with 5 nm of Au/Pd (60:40 ratio) to prevent image charging and distortion.

UV-visible absorption spectra of the $MAPbI_3$ perovskite films were obtained with a Cary 6000i spectrophotometer (Agilent Technologies Inc., USA). The tool was calibrated with a blank quartz substrate between 300 nm and 1200 nm, with a resolution of 1 nm. Samples were fixed onto a mask with a 1 $mm^2$ circular aperture, and the absorption was measured over the range of calibrated wavelengths.

The photocurrent spectroscopy (*i.e.* EQE) was performed on photovoltaic devices and recorded as a function of the wavelength using a Keithley model 236. A 100 W tungsten lamp (Newport) was used as the excitation source and focused through a Princeton Instruments SpectraPro 150 monochromator. The monochromatic light was chopped at around 3 Hz and Stanford Research Systems SR830 model lock-ins were used to monitor the perovskite signal at the chopping frequency. Data were average for 5 s at each wavelength.

Steady-state photoluminescence was measured using a spectrograph (Acton Research SpectraPro 500i) equipped with a Hamamatsu silicon CCD array detector. The materials were excited with the 457 nm line of an argon ion laser.

Photoluminescence spectra and energy-discriminated carrier decay times were measured using standard photoluminescence and time correlated, single photon counting techniques. Specimens were excited in room temperature air by a nominally 635 nm pulsed laser diode (Picoquant P-C-635M and PDL 800-B) operating at 2.5 MHz and $8 \cdot 10^{-5}$ Watts per $cm^2$ average intensity. Photoluminescence spectra near the band edge were measured using a spectrometer (SpectraPro 2750, 500 nm blazed grating) calibrated to persistent Ne lines and a liquid nitrogen cooled Si charged-coupled detector (Princeton Instruments). The time-dependence of the peak photoluminescence wavelength nearest the band edge was measured with a free running Si single-photon detector (Micro Photon Devices) and a PicoQuant PicoHarp 300 counting system. Time-dependent measurements used a 1% count/pulse ratio, and typical instrument response function 1/e decay times are below 1 ns.

All photoluminescence measurements were performed on glass/ITO/PEDOT:PSS/$MAPbI_3$ samples.

Current−voltage measurements were performed using a Keithley model 2400 digital source meter and 300W xenon lamp (Oriel) solar simulator was used for irradiation. The lamp was calibrated with an NREL-calibrated KG5 filtered Si reference cell. *J−V* curves were taken over an active area of 0.2 $cm^2$ from forward to reverse bias sampled at 0.05 V intervals with a 0.1 s delay time at each voltage step before taking data.

Gas phase mass spectrometry was performed using an atmospheric pressure real-time gas analyzer (HPR-20 QIC, Hiden Analytical). The gases were collected through a capillary (QIC HT250, Hiden Analytical) located at the same position than the substrate during the spray and formation of perovskite films (*i.e. a*=4.0 cm).

**Fracture energy measurements.**

After deposition of the perovskite films, PTAA was added as a protective film. Additional bonding layers, 5 nm of chromium and 200 nm of aluminum, were evaporated onto the PTAA surface. The resulting film stack was bonded to a glass beam with a brittle room-temperature cured epoxy adhesive, and cured overnight in a $N_2$ glovebox. Double cantilever beam (DCB) specimens were loaded under displacement control in a thin-film cohesion testing system (Delaminator DTS, Menlo Park, CA) from which a load, *P*, versus displacement, *Δ*, curve was recorded. The fracture energy, $G_c$ ($J/m^2$), was measured in terms of the critical value of the applied strain energy release rate, *G*. $G_c$ can be expressed in terms of the critical load, $P_c$, at which crack growth occurs, the crack length, *a*, the plain strain elastic modulus, *E′*, of the substrates and the specimen dimension; width, *b*, and half-thickness, *h*. $G_c$ is calculated from Eq. (3)[1]:

Eq. (3) $G_c = \frac{12\,P_c^2\,a^2}{b^2\,E'h^3}\left(1 + 0.64\frac{h}{a}\right)^2$.

An estimate of the crack length was experimentally determined from a measurement of the elastic compliance, *dΔ/dP*, using the compliance relationship in Eq. (4):

Eq. (4) $a = \left(\frac{d\Delta}{dP} * \frac{b\,E'h^3}{8}\right)^{1/3} - 0.64 * h.$

All $G_c$ testing was carried out in laboratory air environment at *ca.* 25°C and 40% R.H. The specimen was loaded in tension with a displacement rate of 1.0 μm/s until reaching $P_c$ and then unloaded slightly to determine the compliance before re-loading. This procedure was continued until crack length equals *L-4h*, where *L* is the length of the substrate.

**Methods reference**

1. Kanninen, M. F. An augmented double cantilever beam model for studying crack propagation and arrest. *Int. J. Fract.* **9,** 83–92 (1973).

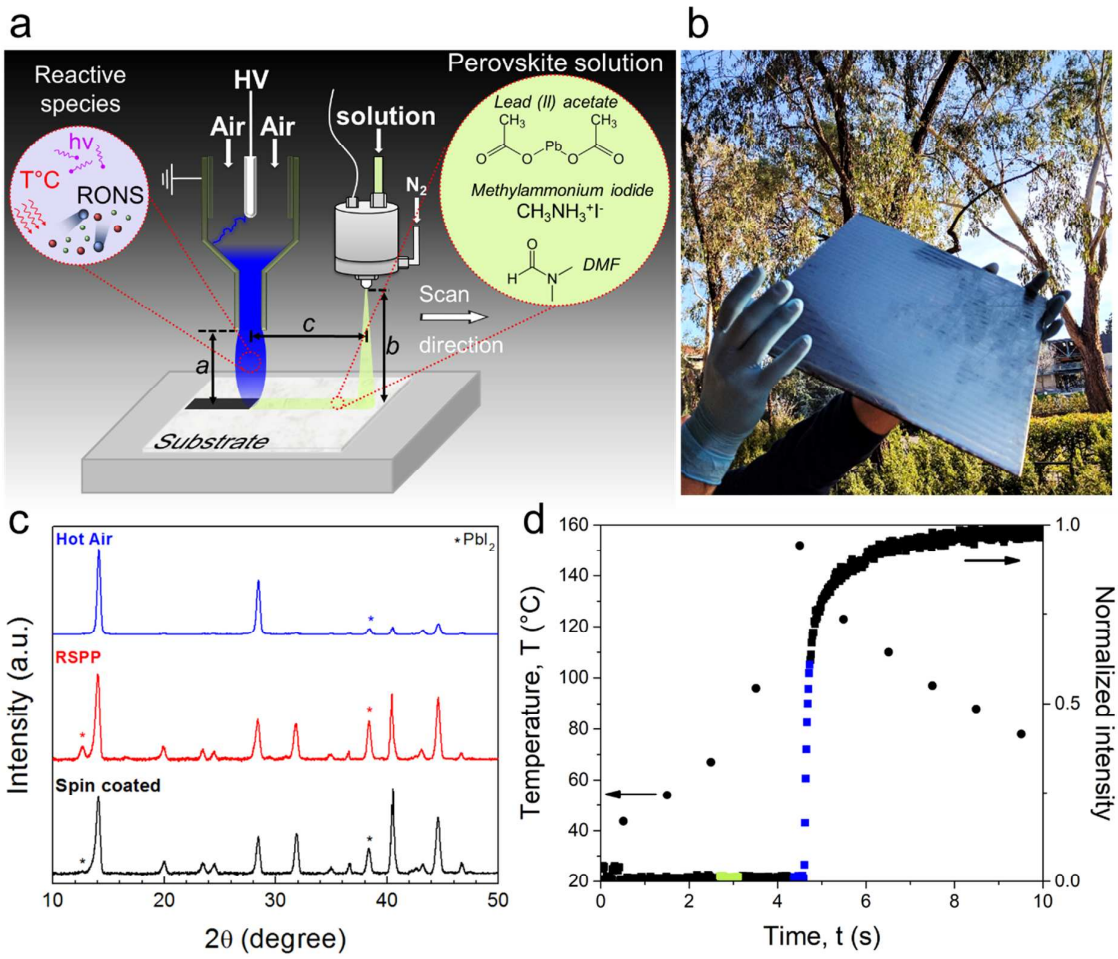

**Figure 1. Material deposition system and thin-film characterization. a**, Atmospheric plasma deposition system for the synthesis of perovskite films. *a* is the plasma nozzle-to-substrate distance, *b* is the spray nozzle-to-substrate distance and *c* is the plasma nozzle-to-spray nozzle distance. **b**, Photograph of a $MAPbI_3$ film deposited by RSPP on a 930 $cm^2$ glass in under 4 min. **c**, X-ray diffraction patterns of the perovskite films deposited by spin coating (black), RSPP (red) and hot air curing (blue). **d**, *In-situ* measurements of: the atmospheric plasma air post-discharge temperature at $a = 4$ cm with a scan velocity of 40 mm/s; the normalized intensity of the (110) peak is representative of the crystallization of the perovskite. The green markers time stamp the spray over the analyzed area and the blue markers time stamp the plasma over the analyzed area.

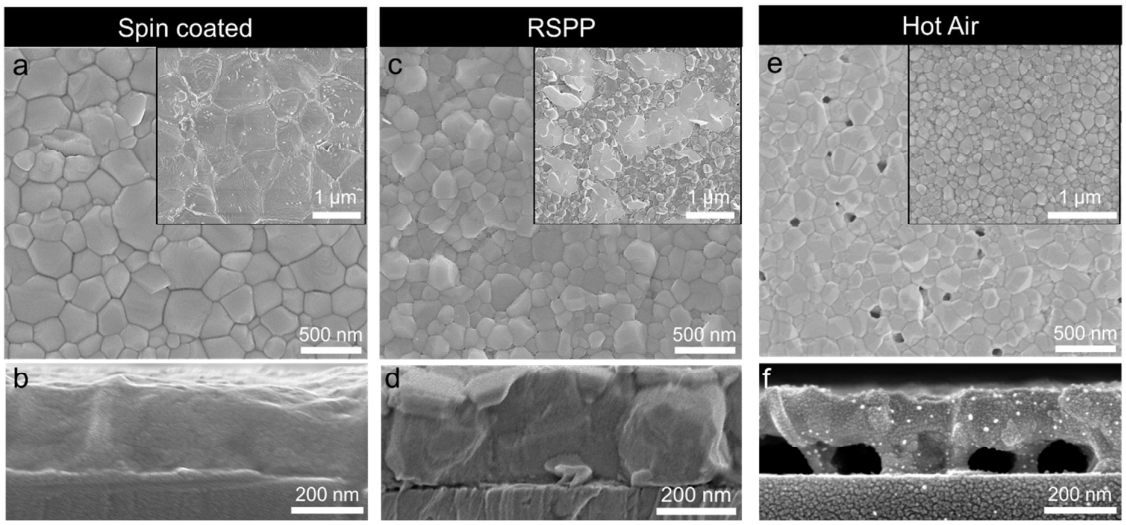


**Figure 2. Thin films morphology and cross-section.** SEM top views of **a**, spin coated, **c**, RSPP and **e**, hot air-cured perovskite films. Cross-sectional SEM images of **b**, spin coated, **d**, RSPP and **f**, hot-air cured perovskite films.

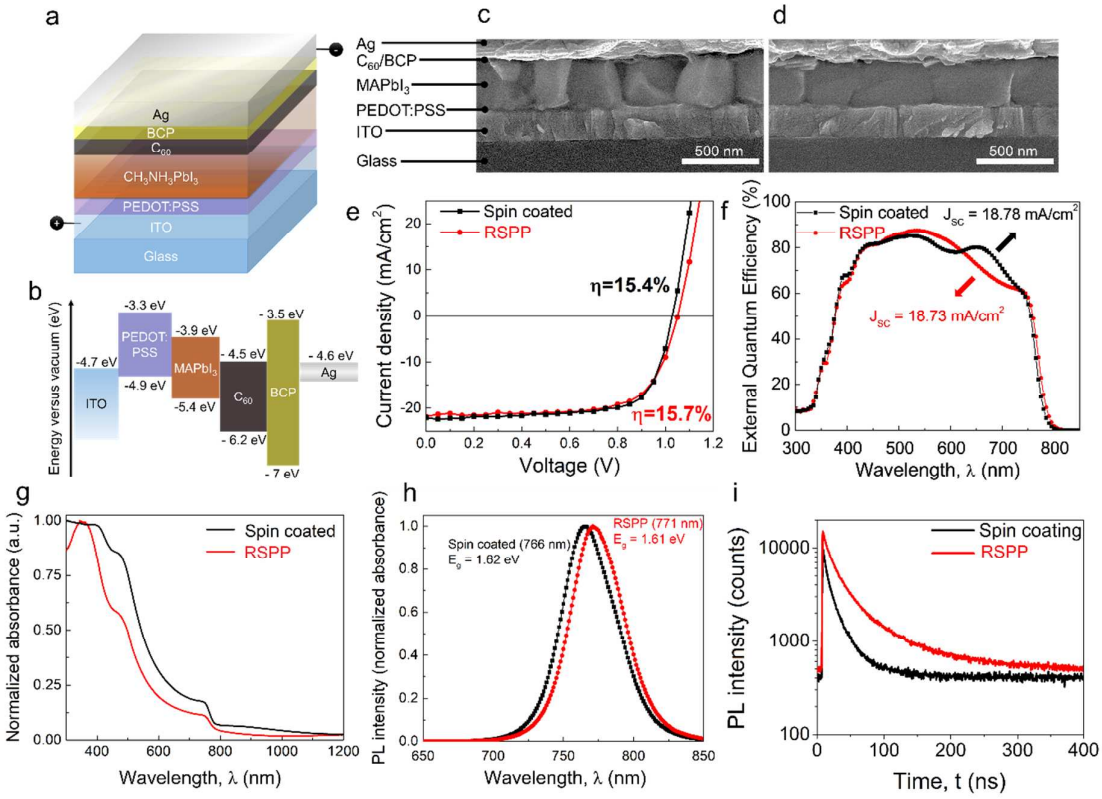


**Figure 3. Solar cell devices performances and optical properties. a**, Schematic illustration of the planar perovskite solar cell architecture used in this study. **b**, Energy-level diagram corresponding to the valence and conduction band of the different layers of materials included in the solar cell devices. Cross-sectional SEM image of complete solar cells elaborated from **c**, RSPP and **d**, spin-coated perovskite film. **e**, Current-density/voltage curve of the best-performing RSPP planar heterojunction perovskite solar cell measured under simulated AM1.5 sunlight of 100 mW·cm$^{-2}$ irradiance. **f**, EQE plots of the spin-coated and RSPP $MAPbI_3$ films. **g**, Absorption spectra of the spin-coated and RSPP $MAPbI_3$ films. **h**, Time-integrated PL spectra and **i**, Time-resolved PL decay transients measured at 765 ± 10 nm for the spin-coated film and at 770 ± 10 nm for the RSPP film.

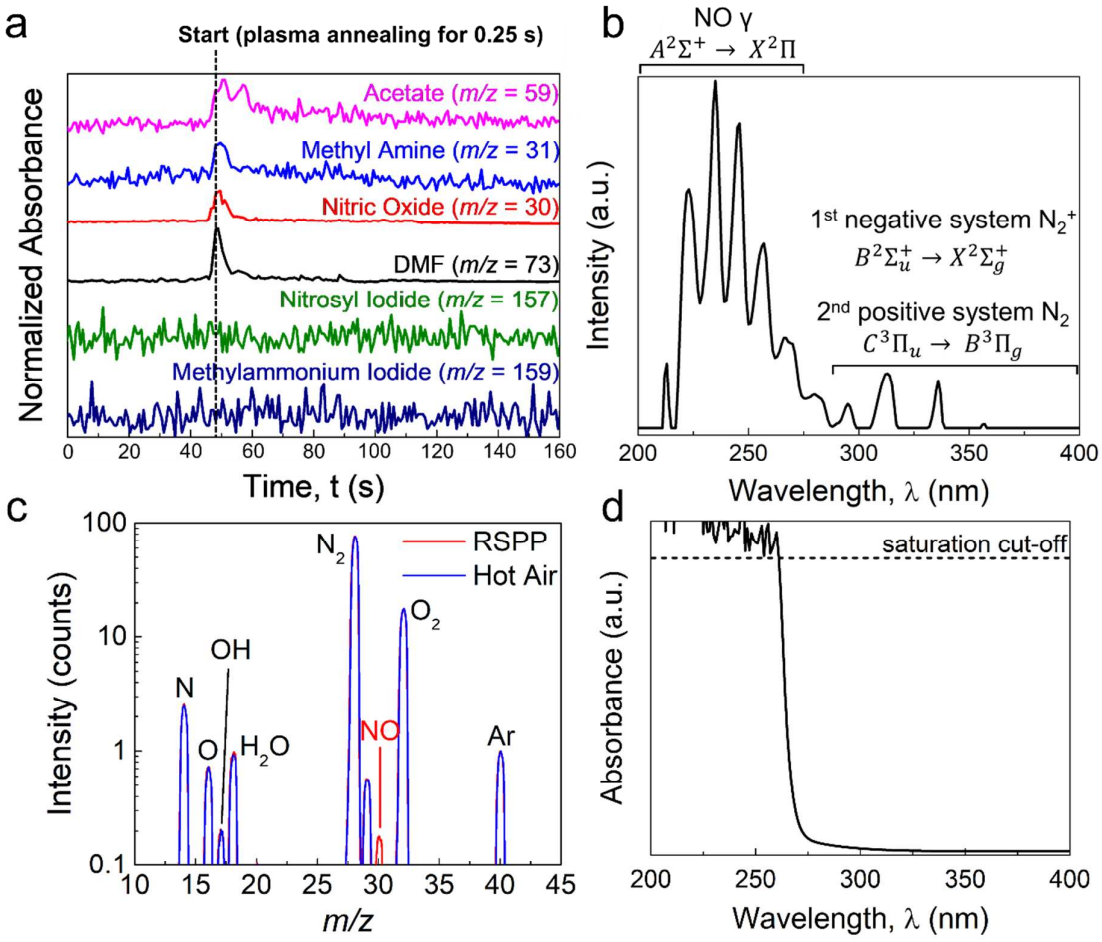


**Figure 4. RSPP reactive species measurements. a**, Time-resolved *in-situ* gas phase mass spectra of elements of interest present during RSPP anneal. **b,** Optical emission spectroscopy spectrum for atmospheric pressure air plasma post-discharge in the UV range. **c**, *In-situ* gas phase mass spectra corresponding to the gas phase of RSPP air plasma post-discharge and hot air in mass range *m/z* = 10-45, showing the presence of NO• radicals only in the RSPP gas phase. **d**, Absorption spectrum of DMF in the UV range.

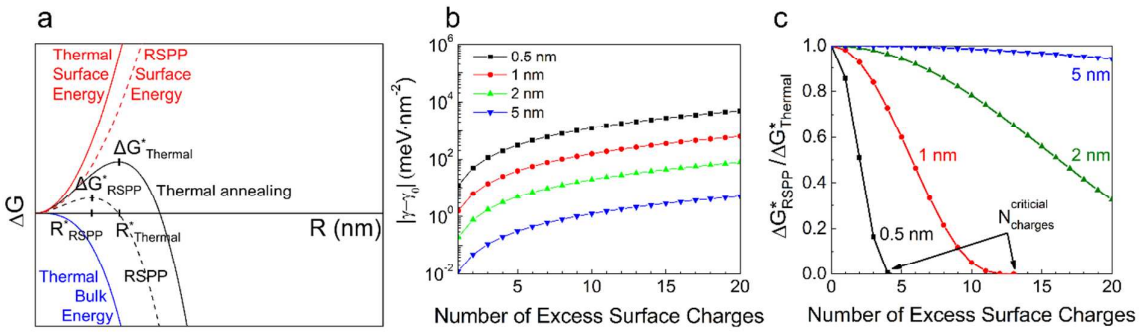


**Figure 5. Nucleation and growth mechanisms. a**, Diagrams representing the nucleation of perovskite for different annealing energies. **b**, Change in surface energy due to the number of excess charged species for different nucleus radii. **c**, Influence of charged species on the activation barrier to nucleation of perovskite for different particle radius. The critical number of charged species ($N_{charges}^{critical}$) represents the number of excess charges needed to overcome the activation energy.

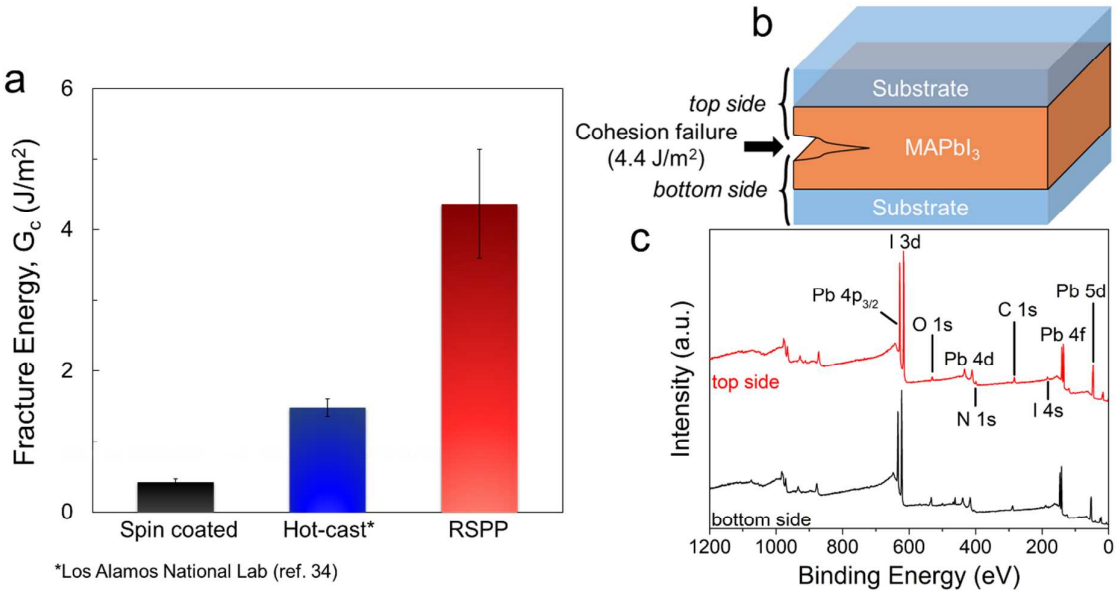


**Figure 6. Fracture energy performances. a**, Fracture energy results. **b**, Architecture of the tested samples showing the cohesion failure within the $MAPbI_3$ perovskite layer. **c**, XPS survey spectra of the fracture halves of the RSPP specimen after delamination.

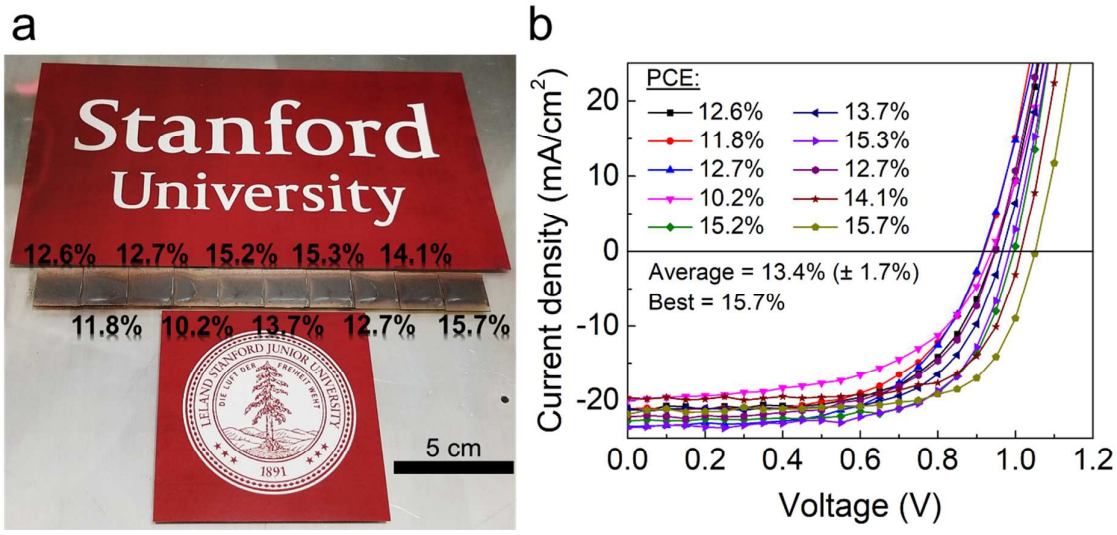


**Figure 7. Large-scale RSPP of $MAPbI_3$.** **a**, Photograph of 10 glass/ITO/PEDOT:PSS substrates coated with $MAPbI_3$ by RSPP in air in 7 seconds and showing the efficiency distribution over the 10 samples. **b**, *J-V* curves associated with the completed devices produced from the 10 samples shown on the left-side picture.